NANO LETTERS
Letter
Cite This: Nano Lett. 2019, 19, 4981−4989
pubs.acs.org/NanoLett

# Optical Control of Non-Equilibrium Phonon Dynamics

Aravind Krishnamoorthy,[†] Ming-Fu Lin,[‡,§] Xiang Zhang,[∥] Clemens Weninger,[‡,§] Ruru Ma,[†] Alexander Britz,[‡,§] Chandra Sekhar Tiwary,[∥,▽] Vidya Kochat,[∥,○] Amey Apte,[∥] Jie Yang,[⊥] Suji Park,[⊥] Renkai Li,[⊥] Xiaozhe Shen,[⊥] Xijie Wang,[⊥] Rajiv Kalia,[†] Aiichiro Nakano,[†] Fuyuki Shimojo,[#] David Fritz,[‡] Uwe Bergmann,[*,§] Pulickel Ajayan,[*,∥] and Priya Vashishta[*,†]

[†]Collaboratory for Advanced Computing and Simulations, University of Southern California, Los Angeles, California 90089, United States
[‡]Linac Coherent Light Source, Stanford Linear Accelerator Center (SLAC) National Accelerator Laboratory, Menlo Park, California 94025, United States
[§]Stanford PULSE Institute, SLAC National Accelerator Laboratory , Menlo Park, California 94025, United States
[∥]Department of Materials Science and NanoEngineering, Rice University, Houston, Texas 77005, United States
[⊥]SLAC National Accelerator Laboratory, Menlo Park, California 94025, United States
[#]Department of Physics, Kumamoto University, Kumamoto 860-8555, Japan

Supporting Information

**ABSTRACT:** The light-induced selective population of short-lived far-from-equilibrium vibration modes is a promising approach for controlling ultrafast and irreversible structural changes in functional nanomaterials. However, this requires a detailed understanding of the dynamics and evolution of these phonon modes and their coupling to the excited-state electronic structure. Here, we combine femtosecond mega-electronvolt electron diffraction experiments on a prototypical layered material, $MoTe_2$, with non-adiabatic quantum molecular dynamics simulations and *ab initio* electronic structure calculations to show how non-radiative energy relaxation pathways for excited electrons can be tuned by controlling the optical excitation energy. We show how the dominant intravalley and intervalley scattering mechanisms for hot and band-edge electrons leads to markedly different transient phonon populations evident in electron diffraction patterns. This understanding of how tuning optical excitations affect phonon populations and atomic motion is critical for efficiently controlling light-induced structural transitions of optoelectronic devices.

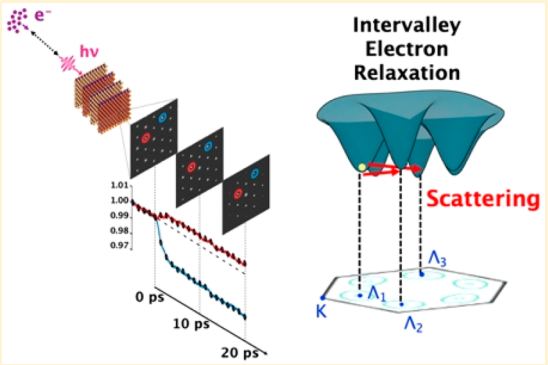


**KEYWORDS:** *Ultrafast electron diffraction, non-equilibrium phonon dynamics, electron−phonon coupling, two-dimensional materials, $MoTe_2$, quantum molecular dynamics*



Light-driven change of crystal structure and symmetry is an emerging method for functionalization of layered and two-dimensional (2D) materials,[1] which are difficult to manipulate via techniques like doping,[2] thermal treatment,[3,4] and strain engineering.[5] Optical excitation can induce irreversible structural changes with high area- and phase-selectivity that are not possible using traditional thermal and strain treatments.[3] Precise control over these structural changes requires an understanding of the interaction between excited charge carriers and transient non-equilibrium phonon populations and dynamics (i.e., electron−phonon coupling), which governs non-radiative energy decay pathways and energy flow into different lattice vibrational modes.[6,7] Previous investigations into non-equilibrium phonon modes focused on the indirect characterization using time-resolved spectroscopy techniques[8,9] and theoretical studies of electron−phonon coupling constants in relation to superconductivity[10,11] and spin and valley polarization.[12] One of the primary challenges for the observation of short-lived non-equilibrium phonon populations is the use of experimental techniques that can resolve atomic structure at picosecond or faster time scales. In this respect, mega-electronvolt ultrafast electron diffraction (MeV-UED)[13,14] is an emerging technique that offers a way to directly probe atomic structure of these crystals in far-from-equilibrium situations with femtosecond time resolution. UED has been previously used to analyze phonon populations in a variety of systems such as 2D and layered materials[15−18] and bulk materials like $SrTiO_3$[19] and aluminum.[11] Such fs−ps characterization of lattice motion enabled by UED experiments

Received: March 21, 2019
Revised: June 12, 2019
Published: June 24, 2019




DOI: 10.1021/acs.nanolett.9b01179
Nano Lett. 2019, 19, 4981−4989

has provided new insights into non-equilibrium dynamics, phonon population, and lattice thermalization[42] and has led to the development of multitemperature models for ultrafast non-equilibrium vibrational processes.[43]

In this work, we perform femtosecond MeV-UED experiments to explore the possibility of controlling the evolution of phonon populations and structure dynamics in the 2*H*-phase $MoTe_2$ system using optical excitation pulses at two different wavelengths ($\lambda$ = 800 and 400 nm). $MoTe_2$ is a prototypical van der Waals layered material belonging to the family of transition-metal dichalcogenides (TMDCs), whose novel physical and electronic properties are promising for constructing nanoscale transistors and optical devices[20,44] and are model systems for studying fundamental physical phenomena such as type-II Weyl semimetallic behavior,[21] gate-dependent collective phenomena, and quantum spin Hall insulating states.[22,23] We demonstrate how tuning the initial photoexcitation energy results in an anisotropic coupling to zone-center and zone-edge vibration modes and thus provides control over the dynamics of energy redistribution and transient non-equilibrium phonon populations in the photoexcited crystal. We use non-adiabatic quantum molecular dynamics (NAQMD) simulations, which can model coupled electron−lattice motion,[24] to identify intravalley and intervalley electron relaxation pathways for hot and band-edge electrons that lead to preferential coupling zone-center and zone-edge phonon modes. Classical molecular dynamics simulations are used to confirm the impact of individual phonon modes on the measured electron diffraction intensities and diffuse scattering patterns.

**Results.** The structural dynamics of $MoTe_2$ following optical generation of hot and band-edge charge carriers are studied directly using the MeV-UED setup as shown in Figure 1. Near-band-edge charge carriers are produced by excitation of multilayer single crystal 2*H*-$MoTe_2$ sample using 1.55 eV photons ($\lambda$ = 800 nm), close to the 1.1 eV indirect bandgap. Hot charge carriers are generated by excitation using 3.1 eV photons ($\lambda$ = 400 nm), which promote electrons from the valence band to empty states deep in the conduction band. In-plane lattice dynamics after excitation are probed in the transmission geometry, with the incident electron beam normal to the (001) plane of the $MoTe_2$ sample. Each MeV-UED snapshot is acquired by the accumulation of over ~10,000 pulses and is used to measure time-dependent intensities of selected lattice planes and other high-symmetry points in the Brillouin zone that can characterize normal vibration modes of the $MoTe_2$ crystal. Diffraction patterns are obtained at a frequency of one snapshot every 0.2 ps (0.4 ps) for a total of 10 ps (20 ps) after the 400 nm (800 nm) optical pump, which enables us to probe electron−phonon and phonon−phonon interactions that occur over the subps and ps time scales. The initial thermalization of photoexcited electrons by electron−electron scattering occurs on time scales of ~100 fs and falls outside the time resolution of our experiments (i.e., full width of half-maximum ~200 fs).[13,25]

All UED snapshots display a six-fold symmetric diffraction pattern characteristic of the honeycomb structure of the 2*H*-phase $MoTe_2$ crystal. The extremely high energy of the incident electrons (3.4 MeV) in our experimental setup allows us to probe a large region of the reciprocal space containing several distinct families of lattice planes like {100}, {110}, {200}, {120}, {300}, {130}, and {220}, which can be resolved above the background noise (Figure 2a). Photoexcitation by 400 and 800 nm optical pulses leads to a strong decrease in the

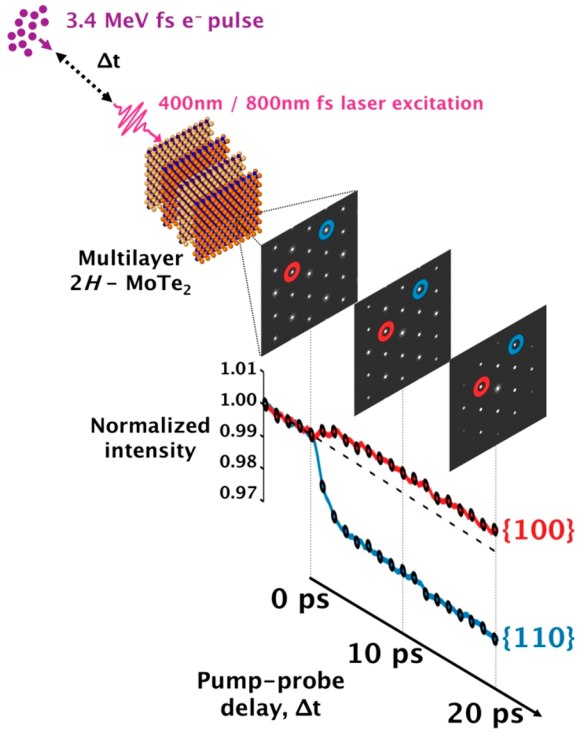


**Figure 1.** Schematic of time-resolved MeV-UED experiments on multilayer 2*H*-phase $MoTe_2$ crystal. Snapshots of electron diffraction of $MoTe_2$ crystal are used to measure lattice plane intensities and momentum-resolved diffuse scattering between diffraction peaks. The graph highlights the difference in the intensity of {100} and {110} families of lattice planes as a function of pump−probe delay time, $\Delta t$, after optical excitation.

intensity of all but one family of lattice planes ({100}) along with an increase in the diffuse scattering in the region of *q*-space between Bragg peaks. Figure 2b,c shows cumulative changes in the UED pattern due to 400 and 800 nm excitation with the relative increase in diffuse scattering and decrease in peak intensities depicted in red and blue, respectively. The decay in lattice plane intensities for both excitation energies (Figure 2d,e) can be modeled using a single exponential decay function and is consistent with increasing disorder in the atomic positions due to an increase in lattice temperature. Quantitatively, the lattice plane intensities $I(q)$ can be explained using the Debye−Waller model, where $\log(I/I_0) \propto q^2$ (Figure 2f, see Supporting Information for more details). This model has successfully been used to explain photoexcited structural dynamics in previous studies.[15,16] Nevertheless, the (100) peak intensity changes induced by the 400 nm pump clearly deviate from the Debye−Waller model, represented by the straight line. This points toward an absolute change of the mean lattice structure.

The intensity of the {100} planes shows an anomalous increase after photoexcitation by the 400 nm optical pulse (Figure 2d) that cannot be explained using increasing lattice disorder and incoherent atomic motion. Anomalous deviation from the Debye−Waller model, including increasing lattice plane intensities, has been observed previously in UED experiments on other materials. These observations are attributed to either changes in the zone-axis due to rotation or warping of the sample,[26] multiple scattering effects,[27] a photoinduced change of crystal symmetry,[28] or some combination of these factors.[29] We do not believe that any


DOI: 10.1021/acs.nanolett.9b01179
Nano Lett. 2019, 19, 4981−4989

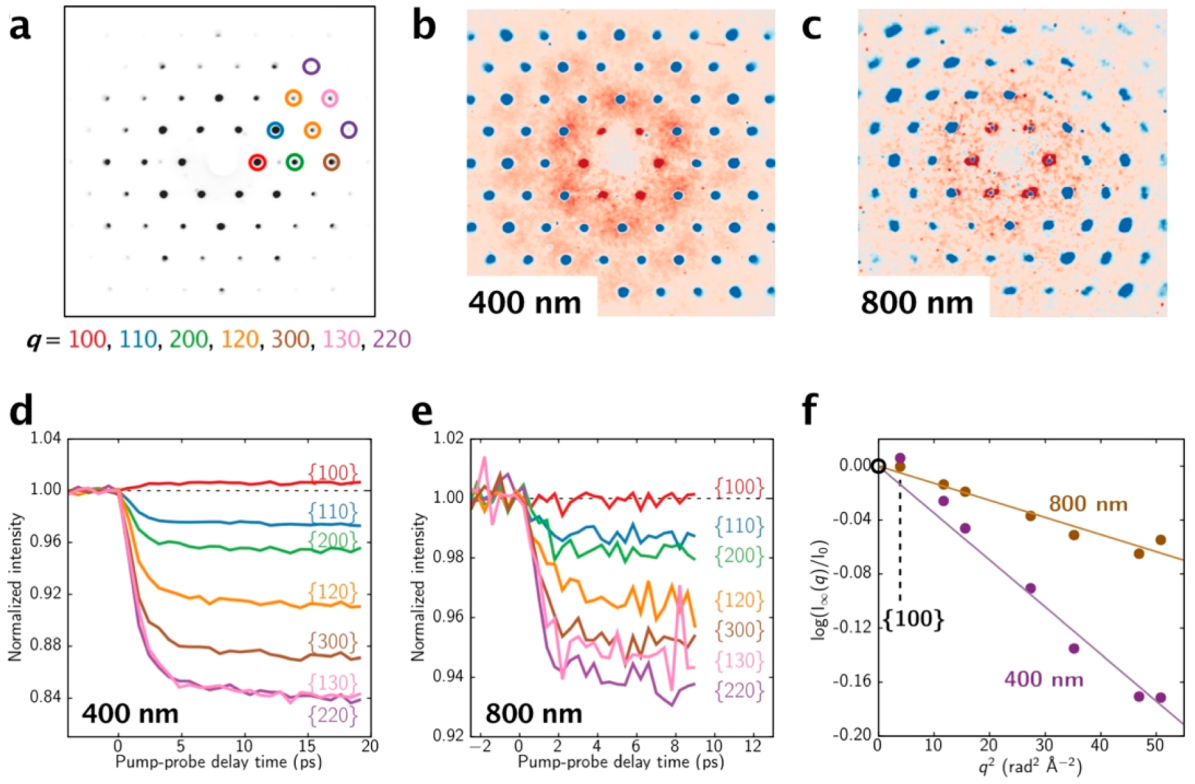


**Figure 2.** (a) Representative UED snapshots of the $MoTe_2$ multilayer during optical excitation. Lattice planes of interest, {100}, {110}, {200}, {120}, {300}, {130}, and {220} are resolvable and highlighted by colored circles. The cumulative difference in UED pattern due to (b) 400 nm and (c) 800 nm excitation shows the pattern of diffuse scattering and the anomalous behavior of the {100} peak intensity. Time profiles of the normalized UED intensity of different planes shows an anomalous increase in the intensity of the {100} plane due to (d) 400 nm excitation, while (e) 800 nm excitation causes only a decay in intensities consistent with lattice thermalization and the Debye−Waller behavior as shown in (f).

of these phenomena are responsible for the observed behavior of the {100} lattice plane intensities. We did not observe any signature of sample rotation due to anisotropic heating of the $MoTe_2$ sample by optical excitation. Specifically, we did not observe a significant drift in the position of {100} lattice planes. The mean square displacement of peak positions, $\langle q^2 \rangle$, remains $<10^{-7}$ rad$^2$ Å$^{-2}$ (Figure S4), precluding the possibility of sample warping due to optical pumping. We also do not consider the multiple scattering effect to be significant in our experiments because the thickness of the $MoTe_2$ samples (~10 nm) is significantly smaller than $2\pi\xi$, where $\xi \approx 2600$ nm is the extinction distance for the isotructural bulk 2*H*-$MoS_2$ crystal,[30] for 3.4 MeV electrons. In this limit, the single scattering kinematical diffraction theory is applicable. Further, the magnitudes of decay in {110} and {200} and other lattice planes are in line with those predicted by kinematical diffraction theory (i.e., single scattering approximation), and this is significantly smaller than the predicted decays by multibeam diffraction theory.[27] Finally, increase in peak intensities can also occur in charge density wave (CDW) materials such as 1T-$TaS_2$,[31] where photoexcitation is known to reverse Peierls distortions and stabilize higher-symmetry crystal structures. However, bulk 2*H*-phase $MoTe_2$ crystals are not Peierls-distorted materials and hence do not undergo CDW melting to a higher-symmetry crystal structure upon photoexcitation.

Figure 3 shows the measured diffuse scattering intensities around the {100} and {110} peaks for $MoTe_2$ samples excited using a 400 nm (Figure 3a,b) and 800 nm (Figure 3c,d) optical pulse, respectively. Specifically, we consider UED intensities at three high-intensity points in the Brillouin zone, namely Λ-point ($q$ = 1/6,1/6,0), M-point ($q$ = 1/2,0,0), and K-point ($q$ = 1/3,1/3,0). For both excitation conditions, the time constants for the diffuse scattering profile at the Brillouin zone edge (i.e., at the M- and K-points) are significantly smaller than those for the Λ-point, consistent with time constants in previous studies on TMDC crystals,[15] indicating a strongly non-equilibrium distribution of phonon states for the first ~3 ps after optical excitation. Further, the measured diffuse scattering time constant for the 800 nm excitation is lower than that for 400 nm excitation, indicating a stronger and faster coupling to zone-edge vibration modes upon near-band-edge excitation.

To understand the source of this anisotropy in electron−phonon coupling to different momenta and the resulting transient phonon populations at different excitation energies, we performed NAQMD simulations on a bulk $MoTe_2$ supercell (Figure S1), which tracks the atomic trajectories as a function of time based on quantum mechanically computed forces. Photoexcitation is modeled as the instantaneous promotion of an electron from the top of the valence band edge to one of the unoccupied Kohn−Sham energy levels in the conduction band. NAQMD simulations are performed for the excitation of one valence electron by 1.3 and 2.8 eV across the 1.1 eV band gap, modeling qualitatively the effect of optical excitation by 800 and 400 nm optical pulses, respectively. The subsequent time evolution of these eigenlevels and their coupling to the lattice are modeled using time-dependent density functional theory (TD-DFT), and non-adiabatic coupling between energy levels is computed using surface hopping. The effective concentration of excited charge carriers



DOI: 10.1021/acs.nanolett.9b01179
Nano Lett. 2019, 19, 4981−4989

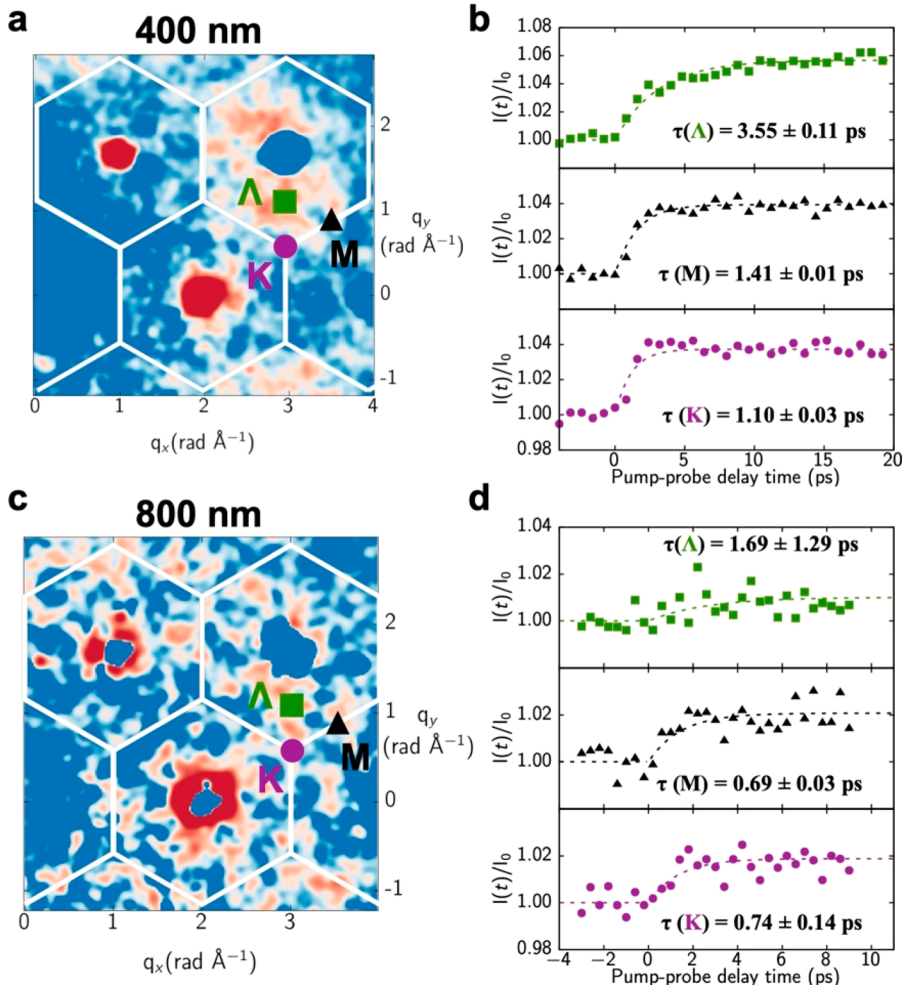


**Figure 3.** Diffuse scattering around the {100} and {110} planes highlighting three high-symmetry $q$ points of interest, Λ(1/6,1/6,0), M(1/2,0,0), and K(1/3,1/3,0), during 400 nm (a) and 800 nm excitation (c). The variation in the time constant at the three high-symmetry $q$ points suggests an anisotropic coupling to different phonon modes and a non-equilibrium distribution of phonons. The 400 nm optical excitation (c) leads to slower coupling to zone-edge phonons at the M- and K-points than the 800 nm optical excitation (d).

in these simulations is 7.5 × $10^{20}$ $cm^{-3}$, which is similar to the estimated carrier density in UED experiments (1.0−6.0 × $10^{20}$ $cm^{-3}$). Figure 4a,b shows the time-dependent Kohn−Sham eigenlevels and the relaxation of the excited electron and hole in two NAQMD simulations, where electron at $t$ = 0 is excited by 1.3 and 2.8 eV, respectively. In both simulations, electron−phonon scattering processes lead to ultrafast relaxation of the hot and near-band-edge electrons down to the conduction band edge within ∼2 ps, consistent with experimental observations in transient absorption experiments on similar TMDC crystals.[32] The single-electron Kohn−Sham energy levels are a functional of the atomic positions in the unit cell. Therefore, the phonon modes in the system and the corresponding periodic (in time) variation in atomic positions will be reflected as modulation in the Kohn−Sham energy levels at the same frequency. A Fourier transform of the Kohn−Sham energy levels can therefore provide information about lattice vibration frequencies in the NAQMD simulation cell, however direct quantification of atomic displacements and phonon populations cannot be inferred directly from this electronic response. Figure 4c,d shows the Fourier transform of the time-dependent Kohn−Sham energy levels upon electronic excitation by 1.3 and 2.8 eV, respectively. The relaxation of the near-band-edge electron from the 1.3 eV excitation couples to the lattice predominantly via low-frequency phonons (Figure 4c) with $\omega$ < 150 $cm^{-1}$, characteristic of the longitudinal acoustic vibration mode at the M point, LA(M). In contrast, the relaxation of hot electrons is dominated by the higher-frequency vibrations ($\omega \approx$ 150−250 $cm^{-1}$, Figure 4d), which are characteristic frequencies of the $E^1_{2g}$ and $A_{1g}$ optical modes (Figure 4g).[33] To understand this anisotropy in phonon populations due to near-band-edge and hot electron relaxation, we calculate phonon dispersion curves (Figure 4e) and electron−phonon coupling constants (Figure 4f) for bulk 2*H*-phase $MoTe_2$ crystals using *ab initio* density functional theory. The energy-resolved Eliashberg spectral function, $\alpha^2F(\omega)$, which measures the strength of the electron−phonon interaction is pronounced near $\omega$ = 225 $cm^{-1}$ and $\omega$ = 175 $cm^{-1}$, corresponding, respectively, to strong coupling to the Raman-active $E^1_{2g}$ and $A_{1g}$ vibrations.[12,34] This strong coupling to the Γ-point optical modes is also supported by the momentum-resolved electron−phonon coupling parameter, $\lambda_q$ which is highest at the center of the hexagonal Brillouin zone (Figure 4h). Electron−phonon coupling at lower frequencies ($\omega \approx$ 75 $cm^{-1}$) is attributed to strong coupling to the zone-edge longitudinal acoustic modes at the M-point, LA(M), consistent with observations from other TMDC systems.[3,15] At even lower frequencies (≈25 $cm^{-1}$), coupling to



DOI: 10.1021/acs.nanolett.9b01179
*Nano Lett.* 2019, 19, 4981−4989

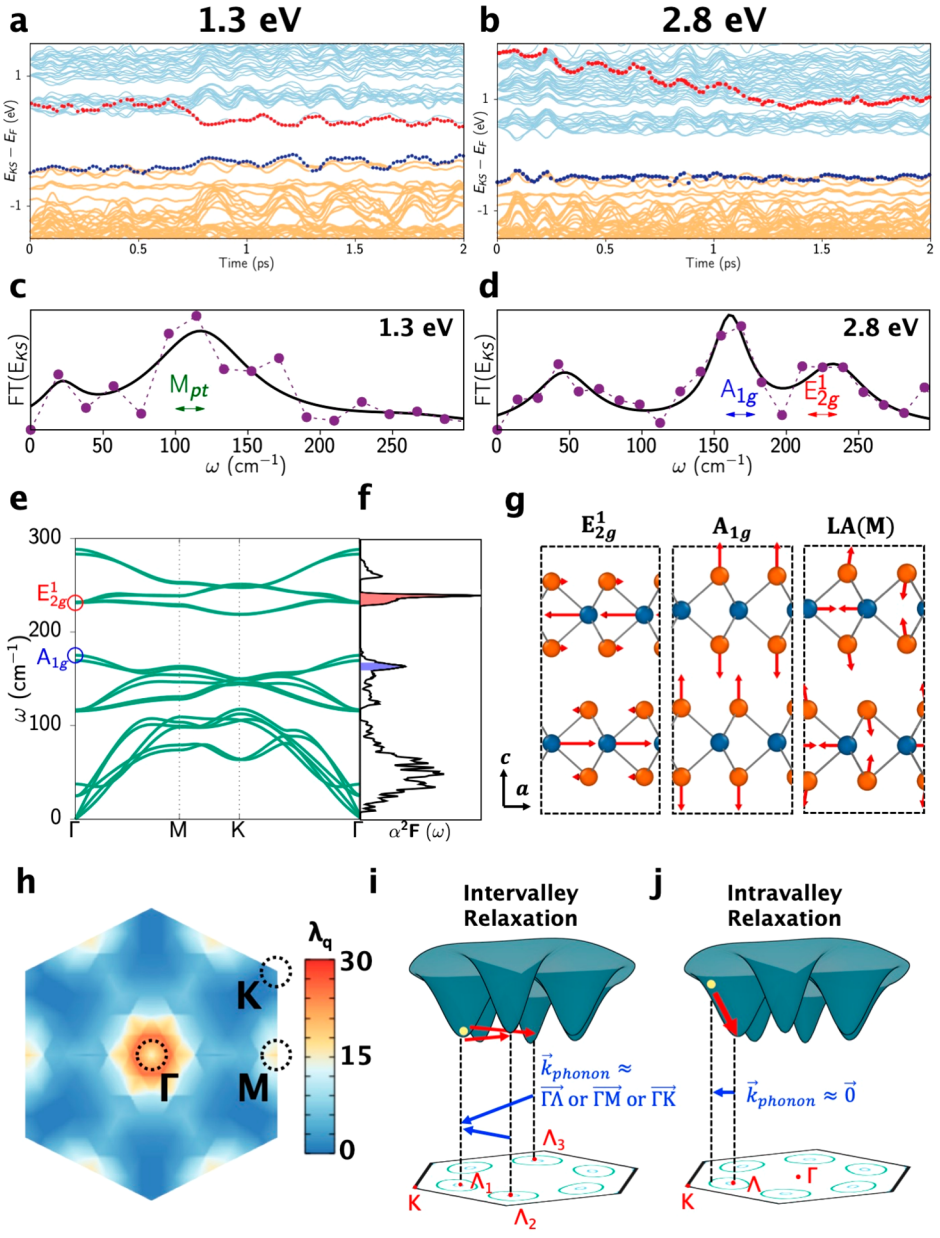


**Figure 4.** Plot of time-dependent Kohn–Sham eigenlevels after excitation by (a) 1.3 eV and (b) 2.8 eV. Blue and red dots in the valence and conduction bands indicate the location of the excited hole and electron, respectively. The Kohn–Sham energy levels are calculated based on the instantaneous position of atoms in the simulation cell, and the dynamics of these levels directly corresponds to dynamics of phonon modes in the system. (c) The Fourier transform of the time-varying Kohn–Sham eigenlevels of the near-band-edge electrons consists primarily of zone-edge acoustic modes, LA(M). (d) The Fourier transform of eigenlevels during hot-electron relaxation contains frequencies corresponding to optical zone-center phonon modes, $E^1_{2g}$ and $A_{1g}$ highlighted in the phonon dispersion curve (e) for bulk $MoTe_2$ crystal. The points in (c) and (d) are the Fourier transform values, and the thick lines are a fit using three Lorentzians as a guide to the eye. The Eliashberg spectral function (f) and the momentum-resolved electron phonon coupling constant, $\lambda(q)$, (h) for bulk $MoTe_2$ show strong coupling at the Γ-point due to $E^1_{2g}$ and $A_{1g}$ vibration modes and longitudinal acoustic modes at the M-point whose eigenvectors are described in (g). Schematic of near-band-edge electron relaxation via intervalley scattering (i) between different Λ-valleys leads to the emission of M-, K-, and Λ-point phonons, while intravalley relaxation of hot electrons (j) leads to the emission of high-energy optical phonons of a negligible momentum.

the interlayer symmetric and asymmetric breathing modes leads to higher values of $\alpha^2F(\omega)$.[35] Figure 4e,f shows the proposed relaxation pathways for near-band-edge and hot electrons, respectively, and their interplay with the strongly coupled phonon modes identified above. Near-band-edge electrons generated by 800 nm photoexcitation lie within one of six degenerate valleys in the conduction band, located at the Σ-point in the Brillouin zone (see Figure S5 for more details about band edges). The primary relaxation pathway for these near-band-edge electrons is intervalley scattering to one of five other valleys in the conduction band, leading to the emission of low-energy band-edge acoustic phonons like LA(M) (Figure 4e). In contrast, the dominant energy relaxation pathway for hot electrons generated by 400 nm photoexcitation is intravalley scattering within a given conduction band valley via coupling to high-energy phonons of vanishing momentum (i.e., optical zone-center phonons like $A_{1g}$ and $E^1_{2g}$, Figure 4f). Coupling to these optical modes



DOI: 10.1021/acs.nanolett.9b01179
Nano Lett. 2019, 19, 4981–4989

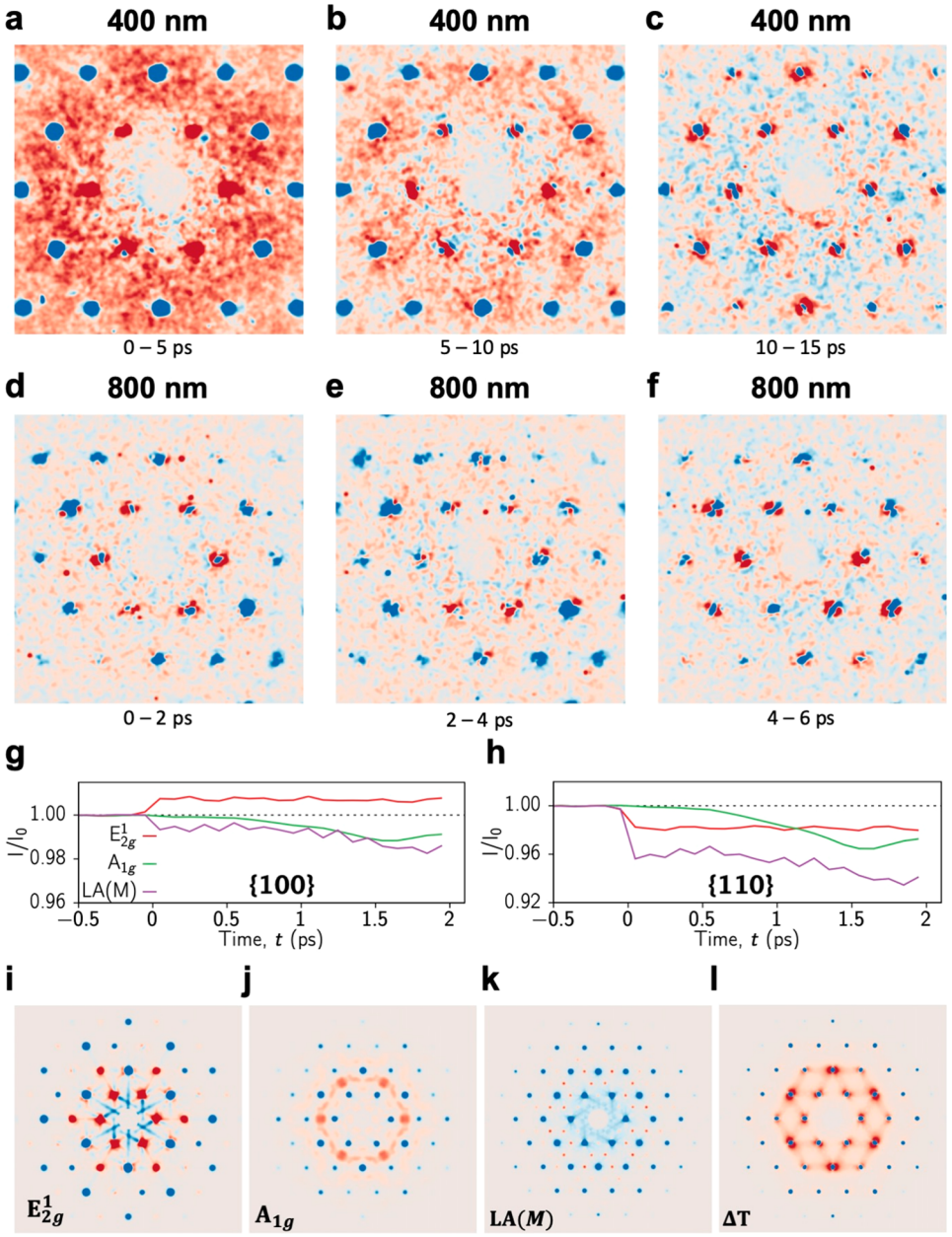


**Figure 5.** Time-resolved diffuse scattering of 2*H*-$MoTe_2$. (a) The instantaneous and short-time scale (0−5 ps) response to 400 nm excitation has two notable features, an increase in {100} intensity and strong diffuse scattering around low-$q$ regions (particularly {100} and {110}). (b) At slightly longer time scales (5−10 ps), UED patterns are characterized by a strong decrease in the intensity of all lattice peaks due to increasing temperature of the crystal. The diffuse intensity is increasingly localized in halos around the {100} and {110} peaks. (c) At even longer time scales (>10 ps), there is no further significant decay in the peak intensities due to the equilibrium of lattice, and diffuse intensity is strongly concentrated in halos around {100} and {110} peaks. (d) The instantaneous response to 800 nm excitation does not show any measurable increase in {100} intensity. Further, diffuse scattering is localized around {100} peak positions, similar to the case of 400 nm excitation at longer time scales. (e, f) The lattice is found to be thermalized within 5 ps, with no significant further decrease in peak intensities. A comparison of the effect of the different phonon modes, $E^1_{2g}$, $A_{1g}$, and LA(M) on the intensity of the (g) {100} and (h) {110} intensities shows that the zone-center mode leads to a ∼1% rise in the intensity of the {100} peak, consistent with observations from the 400 nm excited UED experiments. (i−k) The effects of these three phonon modes on patterns of diffuse scattering, without including the Debye−Waller effect, show features such as increasing intensity of {100} plane and zone-edge intensities. (l) The effect of increasing lattice temperature on the diffuse scattering pattern is marked by a strong halo-like signal around lattice peaks.

dominates until the temperature of the optical phonon reaches that of the excited electron. At this point, other relaxation pathways like emission of acoustic phonons could become active.[25]

Further, the magnitude of electron−phonon coupling at the zone-center and zone-edge has an important implication for the efficiency of energy conversion from the excited charge carriers to the lattice. Strong coupling to zone-center phonons results in complete conversion of absorbed optical energy into atomic motion, leading to greater lattice disordering upon 400 nm optical excitation. In contrast, the relatively smaller zone-edge electron−phonon coupling constants lead only to a partial conversion of optical energy into lattice motion due to 800 nm excitation and a correspondingly smaller increase in



DOI: 10.1021/acs.nanolett.9b01179
*Nano Lett.* 2019, 19, 4981−4989

lattice temperature at 20 ps after optical excitation (See Ref 41 and Section 9 of the Supporting Information). Taken together, the two relaxation pathways and electron−phonon constants provide a way to control the non-equilibrium distribution of phonon modes and their populations using the energy of optical excitation.

These relaxation pathways are supported by an analysis of differential UED patterns at different delay time windows after photoexcitation. Differential UED is the sum of all changes in a measured UED pattern within a given delay-time window and thus provides detailed information about structural changes and phonon emission in the photoexcited crystal within the given delay-time window. Figure 5a−c shows the differential UED pattern for three delay-time windows, 0−5 ps, 5−10 ps, and 10−15 ps after optical excitation by a 400 nm optical pulse. Immediately after excitation, the UED pattern is dominated by a strong rapid rise in the {100} intensity and a uniform increase in the diffuse scattering intensity in the Brillouin zone around the {110} peak, as shown in Figure 5a. At intermediate delay times from 5 to 10 ps, the {100} intensity continues to increase, but the diffuse intensity becomes more localized to regions close to the {110} lattice peak, as shown in Figure 5b. At longer time scales from 10 to 15 ps, the intensity of the {100} planes begins to decrease in intensity, and all diffuse scattering is strongly localized to halos around the lattice positions. These differential UED patterns are consistent with the proposed intravalley energy relaxation pathways for hot electrons, which initially couple to zone-center optical phonons leading to an increase in peak intensities at short time scales, followed by coupling to other vibrational modes as the temperature of the optical mode increases. Phonon dynamics due to an 800 nm excitation is relatively simple and lacks the complex non-monotonic variation of intensities and time-dependent diffuse scattering encountered in hot electron relaxation. Figure 5d−f shows the measured differential scattering at $\Delta t$ = 0−2 ps, 2−4 ps, and 4−6 ps, respectively. During all three time windows, the intensity of all lattice planes including {100} decrease and diffuse scattering is localized to halos around the {100} and {110} peaks.

To understand the impact of individual phonon modes on the measured lattice plane intensities and diffuse scattering patterns, we perform classical molecular dynamics simulations on a laterally large 305 Å × 305 Å 2*H*-phase bulk $MoTe_2$ crystal using a combined Stillinger−Weber and Lennard-Jones force field, parametrized to reproduce the complete phonon dispersion curve (Figure S4). This significantly larger system is required for the analysis of near-zone-center phonon modes, which correspond to long-wavelength collective vibrations spanning several nanometers which are inaccessible in laterally small NAQMD supercells. Phonon emission is modeled in these molecular dynamics simulations through the instantaneous application of a force at $t$ = 0 to all atoms in the system along the eigenvector of the phonon mode. This applied force results in an instantaneous increase in the mean square displacement of atoms at $t$ = 0 (Figure S1). Figure 5g,h shows the effect of three individual phonon modes, high-energy optical $E^1_{2g}$ and $A_{1g}$ and low-energy LA(M) on the intensity of two lattice planes, {100} and {110}. Atomic displacements corresponding to the Γ-point $E^1_{2g}$ mode leads to an 1% increase in the intensity of the {100} lattice plane and a 2% decrease in the intensity of {110} peaks consistent with early stage differential UED patterns due to 400 nm optical excitation and the proposed intravalley relaxation of hot electrons. The two other vibrational modes considered here, $A_{1g}$ and LA(M), lead only to a reduction in both {100} and {110} plane intensities, as observed in UED patterns following 800 nm excitation. The computed diffraction intensities are averaged over 200 fs, equal to the instrument response time, in order to simulate the experimental UED intensities as a function of time. This time-averaging suppresses signatures of coherent oscillations corresponding to the higher-frequency optical $E^1_{2g}$ and $A_{1g}$ modes (Figure S9).

**Discussion.** Our combined ultrafast electron diffraction experiments and non-adiabatic quantum molecular dynamics simulations elucidate how the interplay between the intrinsic electronic structure and the electron−phonon coupling in 2D materials can be exploited to control the phonon distribution after photoexcitation. Hot charge carriers, excited by high-energy photons, relax by coupling strongly to zone-center vibration modes leading to a complete conversion of absorbed optical energy into atomic motion. Excitation of near-band-edge carriers by low-energy photons leads only to the emission of zone-edge acoustic phonons due to weak electron phonon coupling. This control over both the non-equilibrium phonon distribution and populations paves the way for optical control over ultrafast dynamical processes including structural changes and phase transformation pathways engineered through tailored photoexcitation.

**Materials and Methods.** *Sample Preparation and Characterization.* $MoTe_2$ multilayer films are synthesized by tellurization of predeposited Mo films. Mo film was deposited on $SiO_2$/Si by e-beam evaporation, which was then placed into a 1 in. quartz tube for tellurization. Te powder was used as the tellurium precursor and located upstream. $H_2$/Ar (15% $H_2$) was used as the carrier gas during the synthesis. After purging with $H_2$/Ar for 20 min, the furnace temperature was ramped to 700 °C over 15 min and held constant for 2 h before cooling down. The synthesized $MoTe_2$ film was characterized by Raman spectroscopy, X-ray diffraction, atomic force microscopy, X-ray photoelectron spectroscopy, and transmission electron microscopy (see Figure S6). The $MoTe_2$ film was then transferred using a thin layer of PMMA, which was first spin-coated onto $MoTe_2$ at 3000 rpm for 1 min. This structure was floated in a HF solution to dissolve the $SiO_2$ substrate. The PMMA-coated $MoTe_2$ film was transferred to DI water and scooped into a silicon nitride membrane grid. Then PMMA was removed using acetone and isopropyl alcohol.

*UED Experiments.* UED experiments are performed at the mega-electronvolt ultrafast electron diffraction facility at SLAC National Accelerator Laboratory at two distinct experimental conditions: (i) In the 800 nm pump experiments, optical pulses have a duration of ∼30 fs (full width at half-maximum, fwhm) and a pulse energy of 1.66 μJ on the sample. The laser spot size was 300 μm (fwhm), and the electron beam size <100 μm on the sample. We estimate a relative absorption of 17.5% of the 800 nm photons, including substrate effects and applying the saturable absorber model. This results in a carrier density of 6.3 × $10^{20}$ $cm^{-3}$. (ii) During the 400 nm pump experiments, the pump pulse duration was ∼50 fs (fwhm), and the pulse energy was 1.3 μJ on the sample. The laser spot size was increased to 685 μm, in order to match the electron beam size of 250 μm (both fwhm). The increased absorption cross section at 400 nm leads to a relative absorptivity of 40% and a resulting carrier density of 1 × $10^{20}$ $cm^{-3}$. In both experiments, the temporal resolution is limited by the ∼200 fs long (fwhm)



DOI: 10.1021/acs.nanolett.9b01179
*Nano Lett.* 2019, 19, 4981−4989

electron bunch with a charge of ~20 fC. The large electron kinetic energy of 3.4 MeV and the sample−detector geometry allow us to measure a range of momentum transfer, $q$, from 0.5 to 11 $Å^{-1}$.

*DFT Calculation of Electron Phonon Coupling Constants.* Electron−phonon properties were calculated using density functional perturbation theory and the Troullier−Martins norm-conserving pseudopotentials as implemented in the Quantum Espresso DFT program.[36] Cutoff energies of 50 and 400 Ry were used for wave functions and charge densities, respectively. An 11 × 11 × 11 Monkhorst−Pack $k$-point grid with Gaussian smearing of 0.03 Ry was used for the phonon calculations on 3 × 3 × 3 $q$-point mesh, and double $k$-point grid was used in the calculation of the electron−phonon interaction matrix element.

*NAQMD Simulation of Electron Relaxation and Phonon Emission.* NAQMD simulations are performed on a bulk $MoTe_2$ supercell containing 54 atoms, corresponding to 3 × 3 unit cells of the 2-H ground-state bilayer crystal structure. Electronic states were calculated using the projector-augmented-wave method, and projector functions were generated for 4d, 5s, and 5p states of Mo and 3d, 4s, and 4p states of Te. The generalized gradient approximation (GGA) was used for the exchange−correlation energy with non-linear core corrections. The GGA functionals used in this study do not include a Hubbard on-site interaction correction. van der Waals interactions were incorporated based on the DFT-D method. Plane-wave cutoff energies were 25 and 250 Ry for electronic pseudowave functions and pseudocharge density, respectively. The energy functional was minimized iteratively using a preconditioned conjugate-gradient method. More details on the implementation of our NAQMD program can be found in ref 37. While such an instantaneous repopulation of electrons ignores effects related to the interaction of matter with the time varying light field, previous studies have successfully modeled non-equilibrium phonon dynamics, including emission of coherent phonons and squeezed phonon states using techniques that instantaneously change force-constants and phonon dispersion curves and electron−phonon interactions.[38]

*Classical MD Simulations for Variations in Ued Patterns and Lattice Plane Intensities.* Classical MD simulations are performed on a bulk $MoTe_2$ 2$H$ crystal of size 305 Å × 305 Å, containing 49,980 atoms equilibrated at 150 K for 80 ps in the NVT ensemble. After this equilibration, individual phonon modes are activated in the crystal by application of an instantaneous force on each atom in the system directed along the eigenvector of the phonon mode. All MD simulations are performed using the LAMMPS molecular dynamics program[39] with interatomic interactions between the Mo and Te atoms described by classical force fields of the Stillinger−Weber functional form parametrized to reproduce vibrational properties and lattice and elastic constants. Stillinger−Weber force fields have been used to reproduce vibrational properties in other TMDC alloys and heterostructures.[40] Further details about the parametrization of the force field used in this study can be found in Section 4 of the Supporting Information.

## ■ ASSOCIATED CONTENT

### Supporting Information

The Supporting Information is available free of charge on the ACS Publications website at DOI: 10.1021/acs.nanolett.9b01179.

Further details about non-adiabatic quantum molecular dynamics and classical molecular dynamics simulations, preparation and characterization of experimental $MoTe_2$ samples, and detailed analysis of ultrafast electron diffraction experiments to extract time constants and temperature jumps (PDF)

## ■ AUTHOR INFORMATION


### Corresponding Authors

*E-mail: bergmann@slac.stanford.edu.
*E-mail: pma2@rice.edu.
*E-mail: priyav@usc.edu.

### ORCID

Aravind Krishnamoorthy: 0000-0001-6778-2471
Xiang Zhang: 0000-0003-4004-5185
Alexander Britz: 0000-0002-1049-2841
Chandra Sekhar Tiwary: 0000-0001-9760-9768
Aiichiro Nakano: 0000-0003-3228-3896
Priya Vashishta: 0000-0003-4683-429X

### Present Addresses

[▽]C.S.T.: Metallurgical and Materials Engineering, Indian Institute of Technology Kharagpur, West Bengal-721302, India
[○]V.K.: Materials Science Centre, Indian Institute of Technology Kharagpur, West Bengal-721302, India


### Author Contributions

A.K. and R.M. performed NAQMD and MD simulations and DFT calculations. M.-F.L., C.W., A.B., C.S.T., V.K., J.Y., S.P., R.L., X.S., and X.W. performed UED experiments on samples synthesized by X.Z. A.K., R.M., M.-F.L., and A.B. performed data analysis. R.K., A.N., F.S., D.F., U.B., P.A., and P.V. designed the experiment. All authors participated in writing the manuscript.

### Notes

The authors declare no competing financial interest.

## ■ ACKNOWLEDGMENTS

This work was supported by the Computational Materials Sciences Program funded by the U.S. Department of Energy, Office of Science, Basic Energy Sciences, under award no. DE-SC0014607. Simulations were performed at the Argonne Leadership Computing Facility under the DOE INCITE program and at the Center for High Performance Computing of the University of Southern California. The UED work was performed at SLAC MeV-UED, which is supported in part by the DOE BES SUF Division Accelerator and Detector R&D program, the LCLS Facility, and SLAC under contract nos. DE-AC02-05-CH11231 and DE-AC02−76SF00515. Sample preparation and characterizations were performed at Rice University, using the instruments in Ajayan's lab and Shared Equipment Authority (SEA).

## ■ REFERENCES

(1) Mannebach, E. M.; Nyby, C.; Ernst, F.; Zhou, Y.; Tolsma, J.; Li, Y.; Sher, M.-J.; Tung, I. C.; Zhou, H.; Zhang, Q.; et al. *Nano Lett.* **2017**, *17* (12), 7761−7766.
(2) Fiori, G.; Bonaccorso, F.; Iannaccone, G.; Palacios, T.; Neumaier, D.; Seabaugh, A.; Banerjee, S. K.; Colombo, L. *Nat. Nanotechnol.* **2014**, *9* (10), 768−779.
(3) Wang, Z. W.; Li, X. Y.; Zhang, G. Z.; Luo, Y.; Jiang, J. *ACS Appl. Mater. Interfaces* **2017**, *9* (28), 23309−23313.



DOI: 10.1021/acs.nanolett.9b01179
*Nano Lett.* 2019, 19, 4981−4989

(4) Cho, S.; Kim, S.; Kim, J. H.; Zhao, J.; Seok, J.; Keum, D. H.; Baik, J.; Choe, D. H.; Chang, K. J.; Suenaga, K.; et al. *Science* **2015**, *349* (6248), 625−628.
(5) McCreary, A.; Ghosh, R.; Amani, M.; Wang, J.; Duerloo, K. A. N.; Sharma, A.; Jarvis, K.; Reed, E. J.; Dongare, A. M.; Banerjee, S. K.; et al. *ACS Nano* **2016**, *10* (3), 3186−3197.
(6) Nicholson, C. W.; Lucke, A.; Schmidt, W. G.; Puppin, M.; Rettig, L.; Ernstorfer, R.; Wolf, M. *Science* **2018**, *362* (6416), 821−825.
(7) Bernardi, M.; Vigil-Fowler, D.; Ong, C. S.; Neaton, J. B.; Louie, S. G. *Proc. Natl. Acad. Sci. U. S. A.* **2015**, *112* (17), 5291−5296.
(8) Kim, J.; Jin, C. H.; Chen, B.; Cai, H.; Zhao, T.; Lee, P.; Kahn, S.; Watanabe, K.; Taniguchi, T.; Tongay, S.; et al. *Science Advances* **2017**, *3* (7), No. e1700518.
(9) Kozawa, D.; Kumar, R.; Carvalho, A.; Amara, K. K.; Zhao, W. J.; Wang, S. F.; Toh, M. L.; Ribeiro, R. M.; Neto, A. H. C.; Matsuda, K.; et al. *Nat. Commun.* **2014**, *5*, 4543.
(10) Carbone, F.; Yang, D. S.; Giannini, E.; Zewail, A. H. *Proc. Natl. Acad. Sci. U. S. A.* **2008**, *105* (51), 20161−20166.
(11) Li, R. Z.; Zhu, P. F.; Chen, J.; Cao, J. M.; Rentzepis, P. M.; Zhang, J. *Appl. Phys. Lett.* **2017**, *111* (4), 041105.
(12) Shin, D.; Hubener, H.; De Giovannini, U.; Jin, H.; Rubio, A.; Park, N. *Nat. Commun.* **2018**, *9* (1), 638.
(13) Weathersby, S. P.; Brown, G.; Centurion, M.; Chase, T. F.; Coffee, R.; Corbett, J.; Eichner, J. P.; Frisch, J. C.; Fry, A. R.; Guhr, M.; et al. *Rev. Sci. Instrum.* **2015**, *86* (7), 073702.
(14) Shen, X.; Li, R. K.; Lundstrom, U.; Lane, T. J.; Reid, A. H.; Weathersby, S. P.; Wang, X. J. *Ultramicroscopy* **2018**, *184*, 172−176.
(15) Waldecker, L.; Bertoni, R.; Hubener, H.; Brumme, T.; Vasileiadis, T.; Zahn, D.; Rubio, A.; Ernstorfer, R. *Phys. Rev. Lett.* **2017**, *119* (3), 036803.
(16) Lin, M.-F.; Kochat, V.; Krishnamoorthy, A.; Bassman, L.; Weninger, C.; Zheng, Q.; Zhang, X.; Apte, A.; Tiwary, C. S.; Shen, X.; et al. *Nat. Commun.* **2017**, *8* (1), 1745.
(17) Stern, M. J.; de Cotret, L. P. R.; Otto, M. R.; Chatelain, R. P.; Boisvert, J. P.; Sutton, M.; Siwick, B. J. *Phys. Rev. B: Condens. Matter Mater. Phys.* **2018**, *97* (16), 165416.
(18) Chatelain, R. P.; Morrison, V. R.; Klarenaar, B. L. M.; Siwick, B. J. *Phys. Rev. Lett.* **2014**, *113* (23), 235502.
(19) Kohmoto, T.; Tada, K.; Moriyasu, T.; Fukuda, Y. *Phys. Rev. B: Condens. Matter Mater. Phys.* **2006**, *74* (6), 064303.
(20) Li, Y. G.; Li, Y. L.; Araujo, C. M.; Luo, W.; Ahuja, R. *Catal. Sci. Technol.* **2013**, *3* (9), 2214−2220.
(21) Soluyanov, A. A.; Gresch, D.; Wang, Z. J.; Wu, Q. S.; Troyer, M.; Dai, X.; Bernevig, B. A. *Nature* **2015**, *527* (7579), 495−498.
(22) Kim, H. J.; Kang, S. H.; Hamada, I.; Son, Y. W. *Phys. Rev. B: Condens. Matter Mater. Phys.* **2017**, *95* (18), 180101.
(23) Qian, X. F.; Liu, J. W.; Fu, L.; Li, J. *Science* **2014**, *346* (6215), 1344−1347.
(24) Kolesov, G.; Vinichenko, D.; Tritsaris, G. A.; Friend, C. M.; Kaxiras, E. *J. Phys. Chem. Lett.* **2015**, *6* (9), 1624−1627.
(25) Ulstrup, S.; Johannsen, J. C.; Crepaldi, A.; Cilento, F.; Zacchigna, M.; Cacho, C.; Chapman, R. T.; Springate, E.; Fromm, F.; Raidel, C.; et al. *J. Phys.: Condens. Matter* **2015**, *27* (16), 164206.
(26) Park, H. S.; Baskin, J. S.; Barwick, B.; Kwon, O. H.; Zewail, A. H. *Ultramicroscopy* **2009**, *110* (1), 7−19.
(27) González Vallejo, I.; Gallé, G.; Arnaud, B.; Scott, S. A.; Lagally, M. G.; Boschetto, D.; Coulon, P.-E.; Rizza, G.; Houdellier, F.; Le Bolloc'h, D.; Faure, J. *Phys. Rev. B: Condens. Matter Mater. Phys.* **2018**, *97* (5), 054302.
(28) Zong, A.; Kogar, A.; Bie, Y.-Q.; Rohwer, T.; Lee, C.; Baldini, E.; Ergeçen, E.; Yilmaz, M. B.; Freelon, B.; Sie, E. J.; Zhou, H.; Straquadine, J.; Walmsley, P.; Dolgirev, P. E.; Rozhkov, A. V.; Fisher, I. R.; Jarillo-Herrero, P.; Fine, B. V.; Gedik, N. *Nat. Phys.* **2019**, *15*, 27−31.
(29) Wei, L. L.; Sun, S. S.; Guo, C.; Li, Z. W.; Sun, K.; Liu, Y.; Lu, W. J.; Sun, Y. P.; Tian, H. F.; Yang, H. X.; Li, J. Q. *Struct. Dyn.* **2017**, *4* (4), 044012.
(30) Hines, R. L.; Patterson, C. E. *J. Electron Microsc. Tech.* **1985**, *2* (5), 425−429.
(31) Eichberger, M.; Schafer, H.; Krumova, M.; Beyer, M.; Demsar, J.; Berger, H.; Moriena, G.; Sciaini, G.; Miller, R. J. D. *Nature* **2010**, *468* (7325), 799−802.
(32) Seo, M.; Yamaguchi, H.; Mohite, A. D.; Boubanga-Tombet, S.; Blancon, J. C.; Najmaei, S.; Ajayan, P. M.; Lou, J.; Taylor, A. J.; Prasankumar, R. P. *Sci. Rep.* **2016**, *6*, 21601.
(33) Sokolowski-Tinten, K.; von der Linde, D. J. *J. Phys.: Condens. Matter* **2004**, *16* (49), R1517−R1536.
(34) Zhang, J. J.; Gao, B.; Dong, S. *Phys. Rev. B: Condens. Matter Mater. Phys.* **2016**, *93* (15), 155430.
(35) Grzeszczyk, M.; Golasa, K.; Zinkiewicz, M.; Nogajewski, K.; Molas, M. R.; Potemski, M.; Wysmolek, A.; Babinski, A. *2D Mater.* **2016**, *3* (2), 025010.
(36) Giannozzi, P.; Baroni, S.; Bonini, N.; Calandra, M.; Car, R.; Cavazzoni, C.; Ceresoli, D.; Chiarotti, G. L.; Cococcioni, M.; Dabo, I.; Dal Corso, A.; de Gironcoli, S.; Fabris, S.; Fratesi, G.; Gebauer, R.; Gerstmann, U.; Gougoussis, C.; Kokalj, A.; Lazzeri, M.; Martin-Samos, L.; Marzari, N.; Mauri, F.; Mazzarello, R.; Paolini, S.; Pasquarello, A.; Paulatto, L.; Sbraccia, C.; Scandolo, S.; Sclauzero, G.; Seitsonen, A. P.; Smogunov, A.; Umari, P.; Wentzcovitch, R. M. *J. Phys.: Condens. Matter* **2009**, *21* (39), 395502.
(37) Shimojo, F.; Hattori, S.; Kalia, R. K.; Kunaseth, M.; Mou, W. W.; Nakano, A.; Nomura, K.; Ohmura, S.; Rajak, P.; Shimamura, K.; Vashishta, P. *J. Chem. Phys.* **2014**, *140* (18), 18A529.
(38) Johnson, S. L.; Beaud, P.; Vorobeva, E.; Milne, C. J.; Murray, E. D.; Fahy, S.; Ingold, G. *Phys. Rev. Lett.* **2009**, *102* (17), 175503.
(39) Plimpton, S. *J. Comput. Phys.* **1995**, *117* (1), 1−19.
(40) Apte, A.; Krishnamoorthy, A.; Hachtel, J. A.; Susarla, S.; Idrobo, J. C.; Nakano, A.; Kalia, R. K.; Vashishta, P.; Tiwary, C. S.; Ajayan, P. M. *Chem. Mater.* **2018**, *30* (20), 7262−7268.
(41) Kiwia, H. L.; Westrum, E. F. *J. Chem. Thermodyn.* **1975**, *7* (7), 683−691.
(42) Chase, T.; Trigo, M.; Reid, A. H.; Li, R.; Vecchione, T.; Shen, X.; Weathersby, S.; Coffee, R.; Hartmann, N.; Reis, D. A.; Wang, X. J.; Durr, H. A. *Appl. Phys. Lett.* **2016**, *108* (4), 041909.
(43) Waldecker, L.; Bertoni, R.; Ernstorfer, R.; Vorberger, J. *Phys. Rev. X* **2016**, *6* (2), 021003.
(44) Zhang, X.; Jin, Z.; Wang, L.; Hachtel, J. A.; Villarreal, E.; Wang, Z.; Ha, T.; Nakanishi, Y.; Tiwary, C. S.; Lai, J.; et al. *ACS Appl. Mater. Interfaces* **2019**, *11*, 12777−12785.



DOI: 10.1021/acs.nanolett.9b01179
*Nano Lett.* 2019, 19, 4981−4989